

Drying drops

Drying drops containing solutes: From hydrodynamical to mechanical instabilities

F. Giorgiutti-Dauphiné^a and L. Pauchard^b

Laboratoire F.A.S.T, UMR 7608 CNRS - Univ. Paris-Sud, Université Paris-Saclay, 91405, Orsay CEDEX, France

Received 16 January 2018 and Received in final form 13 February 2018

Published online: 19 March 2018 – © EDP Sciences / Società Italiana di Fisica / Springer-Verlag 2018

Abstract. The drying of complex fluids involves a large number of microscopic phenomena (transport and organization of non-volatile solutes) as well as hydrodynamic and mechanical instabilities. These phenomena can be captured in drying sessile drops where different domains can be identified: strong concentration gradients, formation of a glassy or porous envelope that withstands mechanical stress, and consolidation of a layer strongly adhering to the substrate at the drop edge. In colloidal systems, we quantify the evolution of the particle volume fraction at a nanometric scale and microscopic scale and identify the conditions for the envelope formation at the free surface by balancing the effect of diffusion and evaporation. When a solid envelope is formed at a drop surface, the mechanical instabilities induced by the drying result in different drop shapes. Finally, large drying stresses build up in the solid layer adhering on the substrate, and possibly cause crack formation. In particular, we study how crack patterns are affected by the contact angle of drops and the drying conditions. A particular interest of the review is devoted to drying pattern of solutes.

1 Introduction

Drying complex fluids as polymer solutions or colloidal dispersions is a fascinating phenomenon. In its common realization, it transforms a liquid phase into a dense, or porous, solid. In materials science, drying processes are often used to create coatings on the surfaces of solid materials. Typically, a liquid dispersion of non-volatile solutes is applied to the surface of the solid; then, the liquid phase is evaporated to yield a dense solid film. The evaporation of liquid dispersions to create particulate solids is a critical step in the industrial production of high-performance coatings such as optical coatings on glass, porous coatings, paints for the car industry, coatings for microelectronics and cosmetics. In all these technologies, the formation of films from colloidal dispersions is a process of ever increasing importance. Food industry is concerned too as the fabrication of dried milk usually requires the transformation of liquid droplets into a powder form using nozzles; liquid food concentrate is atomized into droplets using spray-drying processes [1–3]. Particularly functional properties have to be controlled such as dispersibility, and solubility that is essential for the capability of the powder to be re-hydrated. Therefore, the droplet morphology or the droplet size changes have to be controlled and the effects of various initial or environmental conditions on a single droplet development have to be understood. In another

area, recent interests have emerged in interpreting solute patterns of evaporated biological fluid droplets for medical screening and diagnostic purposes [4] or in forensics [5]. Understanding this broad variety of shapes is highly relevant for many industrial processes and they represent also a particularly spectacular example in the growing field of surface instabilities.

The presence of non-volatile compounds in the droplet brings considerable changes in the desiccation processes, and leads to hydrodynamical and/or mechanical instabilities that usually need to be controlled.

In this way, at each stage of the drying process, a large number of microscopic phenomena (transport, organization) is involved and is related to instabilities at a macroscopic scale.

Transport of solvent drives the non-volatile solutes. In this configuration, diffusion processes and drying kinetics have been carefully studied [6–8]. Over the last decade, there has been a great deal of scientific and technological interests in studying the flow of materials in drying drops [9]. The resulting Rayleigh-Bénard or Bénard-Marangoni instabilities then modify the shape evolution of the drying drops [10].

At the evaporation surface, concentration gradient modifies the rheological properties of the medium and possibly causes skin formation at the free surface of the medium [11]. When its structural strength is sufficient, the skin can withstand internal stress and can be regarded as an elastic shell confining a liquid phase. This is often responsible for strong distortions of the droplet [12, 7]. In

^a e-mail: fred@fast.u-psud.fr

^b e-mail: pauchard@fast.u-psud.fr

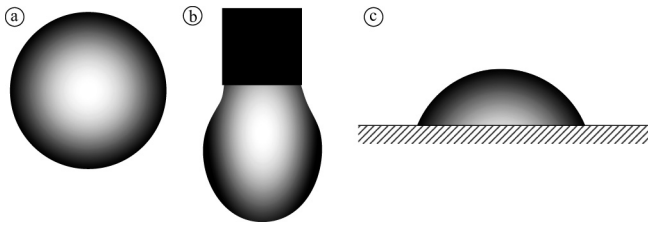


Fig. 1. (a) Spherical drop; (b) pendant drop; (c) sessile drop.

this way deformation of nearly spheroidal droplets were considered in the case of polymer solutions [12] or colloidal dispersions [13, 14]: the various shapes have been related to the buckling process of a skin formed at the drop surface. During the solidification, strong capillary forces are generated and responsible for stress development. For instance, the capillary forces that are generated during evaporation of a nanometric dispersion are huge, on the order of 10^8 Pa. In turn, these capillary forces can generate instabilities in the solid network of particles, creating “drying patterns” on the substrate (inhomogeneous compression and cracking), when stresses exceed the strength of the material.

Drops are usually considered through the following configurations (see sketches in fig. 1). i) Spherical drops usually formed by industrial spray drying or through levitation processes in Leidenfrost condition when a drop on a very hot solid levitates, owing to the presence of a vapour cushion below, or by acoustic levitation, *e.g.*, container-free condition. Since the levitation process avoids the possible contamination of the liquid with container walls or a substrate, this technique is used in a wide range of applications, from pharmaceuticals to bulk commodities such as dried milk drops [15, 16]. ii) The geometry of pendant drop, or suspended drops, is a method used to measure interfacial tension. Moreover the pendant drop is a way to mimic spray drying in a single drop situation resulting in different drop shapes. iii) Sessile drop is apparently the easiest geometry to reproduce but the most difficult to be controlled: the complexity is mainly due to the singularity of the contact line. That is why the review will be devoted to detail recent investigations about sessile droplets. Experiments on droplets are conducted under natural or free convection at ambient temperature, as well as under forced convection at more elevated temperatures, depending on the practical applications. To highlight the physical insights of the recent works on drying droplets, the review will mainly consider the conditions approaching natural droplet evaporation.

The present review will focus on the following items:

- During deposition, liquid dispersions can exhibit all sorts of hydrodynamic instabilities under the effect of applied forces, surface tension and gravitation.
- Evaporation may cause capillary flows that will carry particles across the drops and accumulate them at the liquid/solid contact lines.
- Evaporation will also create concentration gradients that evolve into a skin covering the film or into a drying front that sweeps across the film.

- After solidification, capillary forces build up stresses that cause the propagation of cracks in films made of hard colloidal particles.

2 Evaporation and flows inside the drop

2.1 Evaporation

In the case of spherical drops, evaporation in an ambient gas was theoretically considered and described by Maxwell mainly as diffusion of vapor from a near-surface layer [17]. The first observation during the evaporation process concerns the change of position of the liquid-vapour interface together with the decrease of the drop volume. The rate at which the volume decreases is determined by the diffusive transport of the vapour in the air surrounding the drop. A simple and physical way to deal with the evaporation rate of a drop of characteristic size R is to consider the following timescales. Firstly, the timescale related to the transport of vapour into the gas phase:

$$t_{vap} = R^2/D_{vap}, \quad (1)$$

where D_{vap} is the diffusion coefficient of vapour in the ambient atmosphere (typical value of D_{vap} for water into air at room temperature is: $25 \times 10^{-6} \text{ m}^2 \text{ s}^{-1}$); this timescale is related to the build-up of the concentration profile around the drop by diffusion.

Secondly, the evaporation time t_E describes the rate of volume variation of the drying drop. This timescale essentially depends on both the drop size, R , and the evaporation rate from the drop surface, V_E , and expresses as

$$t_E = R/V_E. \quad (2)$$

This timescale gives the order of magnitude of the duration needed for the drop to completely dry. The characterization of the evaporation rate lies in the determination of the humidity rate, RH , that is determined from the vapour concentrations in air at infinity, $n_{v\infty}$, and at saturation, n_{vs} , that is close to the drop surface (both expressed in moles per unit volume). In this way, RH is a measure of the current amount of water vapor in the air relative to the total amount of water vapor that can exist in the air at its current temperature. The vapour concentration in the vicinity of the liquid-vapour interface is time-dependent and obeys to the unsteady diffusion equation. However, when evaporation is limited by diffusion in the air, $t_{vap}/t_E \ll 1$, quasi-stationary conditions can be assumed. Consequently, the vapour concentration in air n_v follows the Laplace equation $\nabla^2 n_v = 0$. The gradient in vapour concentration governs the radial evaporative flux as

$$J(r) = -D_{vap} \frac{dn_v}{dr}. \quad (3)$$

In the case of a spherical drop, the vapour isoconcentration surfaces are spherical; the radius, r_{iso} , of the surfaces satisfies: $4\pi r_{iso}^2 J(r) = a$, where a is independent of r (fig. 2(a)). Using appropriate boundary conditions, the

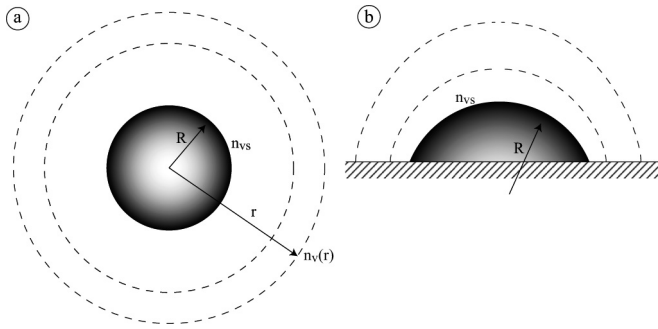


Fig. 2. Sketches of surfaces of equal concentration in vapour in the surroundings of (a) a spherical drop and (b) a sessile drop.

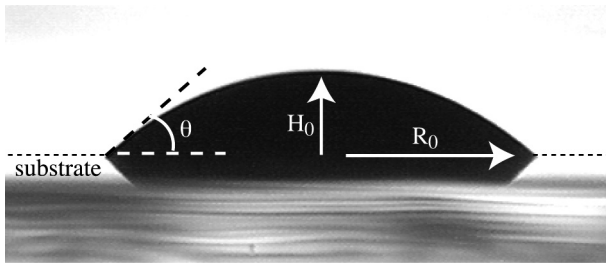


Fig. 3. Image in side view of a sessile drop (the reflected part of the drop by the substrate is clearly observed).

conservation of water flux at the drop surface, $r = R$, gives the evaporation rate from the drop surface:

$$J_s = \frac{D_{vap}}{R} \frac{n_{vs} - n_{v\infty}}{n_1}, \quad (4)$$

where n_1 is the concentration of pure liquid.

In particular, a recent model has shown that the local dependence of the physicochemical properties of the gas with the gas temperature turns out to have a significant influence on the evaporation process at high temperatures [18].

The case of a sessile drop is more complicated due to the existence of the contact angle. This geometry is often encountered and needs a deeper analysis. After the deposition stage during which the droplet spreads on the substrate, an equilibrium is reached: in this way the contact angle at the three-phase line is a characteristic of the wetting of the liquid on the substrate and is determined at a macroscopic view by the surface energies of solid-vapour, solid-liquid, and liquid-vapour surfaces. The contact angle, θ , and the capillary length, defined as $l_c = \sqrt{\gamma/(\rho g)}$ (γ being the liquid-air surface tension, ρ being the density and g the gravitational acceleration), determine the geometrical shape of the drop (fig. 3).

Generally, the solvent removal can lead to a constant contact base induced by a pinned contact line or a constant contact angle with a receding contact line. As an example, the desiccation of a pure water drop is described by dimensionless profiles recorded and superposed at different times in fig. 4. Following the deposition on the substrate, the drop shape exhibits a spherical cap, if $R_0 < l_c$: the drop recedes with a constant contact angle and the

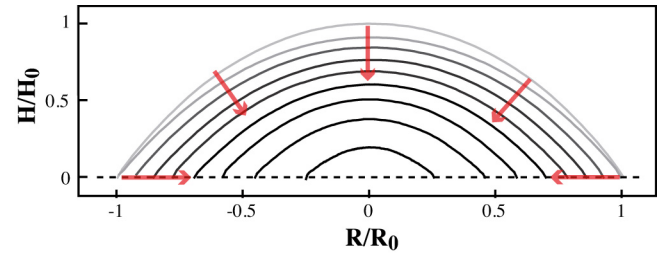


Fig. 4. Time evolution of a sessile drop of pure water (initial volume $5 \mu\text{l}$): dimensionless profiles recorded at different times during the evaporation in ambient air (the substrate, glass slide, is indicated by the dashed line).

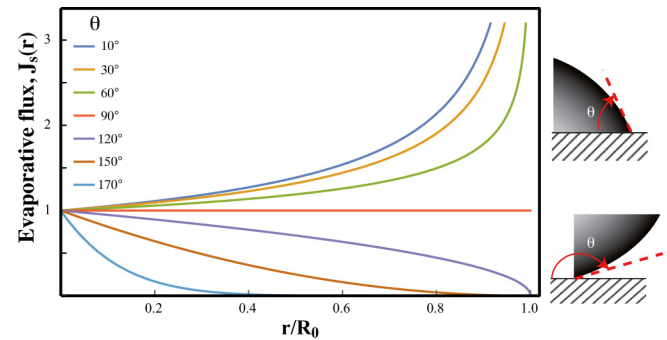


Fig. 5. Dimensionless profiles of the local diffusive evaporation flux for various contact angles.

drop shape remains that of a spherical cap to minimize its superficial energy.

This behaviour is naturally affected by the interaction between the liquid and the substrate. In particular, the influence of the surface properties of substrates on the three-phase line motion was experimentally investigated by considering droplets of pure solvents [19].

In addition to the substrate properties, the complexity of the drying of sessile drops lies mainly in the singularity located at the three-phase line. Although for a spherical droplet, the local evaporation flux profile is uniform at the liquid/air interface, the situation is considerably different in the presence of a substrate. Due to the contact line, the isoconcentration surfaces are not spherical anymore as a result of the boundary condition imposed by the substrate (fig. 2(b)). Indeed, for a sessile droplet with a contact angle less than 90° , the evaporation flux is greatest at the contact line. Physically, if the contact line is pinned, a strong radial flow is generated in order to replenish the liquid removed by evaporation at the drop edge. Then, the local evaporative flux expresses as [20]:

$$J_s(r) \sim \frac{D_{vap}}{R_0} \frac{n_{vs} - n_{v\infty}}{n_1} \left(\frac{R_0}{R_0 - r} \right)^{\frac{\pi - 2\theta}{2(\pi - \theta)}}, \quad (5)$$

where r is the radial distance from the drop centre to the three-phase contact line. Accordingly with eq. (5), profiles of the local diffusive evaporation are plotted for various contact angles in fig. 5. It can be noted that for contact angles larger than 90° , the evaporation flux is maximum at the apex of the sessile drop and minimum at the triple

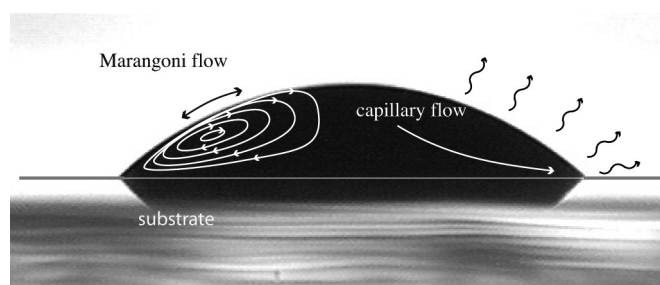


Fig. 6. Streamline plots of the Marangoni flow and capillary flow.

line. This can be understood since the molecules cannot easily leave the triple line due to the very tiny gap between the interface and the surface [21].

2.2 Flow inside a sessile drop

While evaporation converts volatile solvent from a liquid to a gas phase, heat and mass convections take place within the drying drop resulting in local flow fields. The flow inside the drop is governed by the evaporation rate, in particular at the singular drop edge region. Also, this flow field strongly depends on the drop geometry, the motion of the boundary conditions (contact line and liquid/air interface). The flow fields can have different origins: the capillary flow generally causes radial internal flows while Marangoni flow results in loops (fig. 6). Both types of flows are commonly observed in drying drops; in the case of sessile drops of non-volatile solutes, the flow fields are of great importance for the technical control of deposit morphologies.

For small contact angle, the evaporation induces outward flow, *e.g.* capillary flow, directed towards the contact line. In the case of a pinned contact line, this capillary flow replenishes the faster liquid loss at the drop edge, while the contact angle decreases. Therefore, the intensity of the capillary flow depends on the evaporate rate at the drop edge. For thin drop edge, the capillary flow dominates the Marangoni flow.

The Marangoni convection results from the surface tension gradient along the free surface of the drop, and strongly affects the internal flow fields (fig. 6). The surface tension gradient results from two causes: i) a local change of composition (the so-called solutal Bénard-Marangoni convection), and ii) a temperature gradient (the so-called thermal Bénard-Marangoni convection).

i) *Solutal convection.* The solutal convection has been investigated in solvent mixtures [22,23] and in the presence of surfactants [24–26]. In the last case, the local concentration of the surfactant increases towards the contact line due to the capillary flow; this reduces the surface tension at the drop edge and consequently creates a Marangoni flow toward the centre of the drop.

ii) *Thermal convection.* Evaporation is endothermic as it requires energy for the phase change. Indeed, molecules of the liquid phase need to overcome the energy barrier to evaporation before they can change phase and cross the liquid-vapour interface. Molecules with the highest ther-

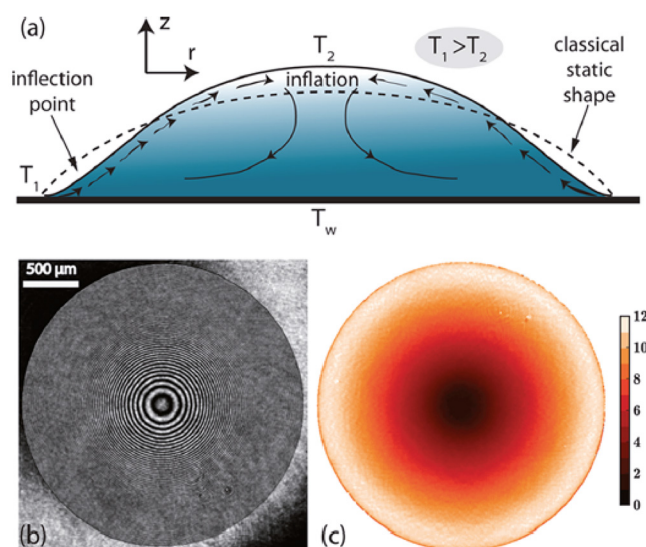


Fig. 7. (a) Sketch illustrating the role of a radially outward surface Marangoni flow on the sessile droplet shape. (b) The typical interference pattern of a sessile drop obtained using an interferometer. (c) Image process of the interference pattern with the contours corresponding to the local slope of the drop indicated in degrees. Reprinted with permission from [27] (Copyright (2015) American Chemical Society).

mal energy can cross the liquid-vapour interface, and consequently, the drop becomes colder. Thus surface tension is strongly affected by temperature, surface tension being lower where the temperature is higher. In this way, a temperature gradient along the drop interface brings up tangential stress. The so-called thermal Marangoni flows may arise from a change of temperature of the substrate, or through an evaporation process that cools the free surface. As an example, the shape distortion during the drying process of a pure solvent is shown in fig. 7. The dimple and the shape inflation are related to evaporation-induced Marangoni flow, directed at the free surface toward the apex of the droplet [27].

Marangoni convection in evaporating sessile water droplets was evidenced by Xu *et al.* [28] using seeding fluorescent nanoparticles. The existence of a stagnation point has also been pointed out on the interface where the surface flow, surface tension, and interfacial temperature gradients change direction. Moreover, Hu *et al.* [29] experimentally and numerically revealed the effect of the thermal Marangoni convection on the deposition morphology in colloidal droplets.

Finally, the combination of solutal and thermal Marangoni effects on the flow fields was experimentally investigated by Ishizuka *et al.* [30]. Marangoni and capillary flow generally compete and result in complex internal flow fields.

3 Vertical and horizontal drying of sessile drops of solutes

For a sessile drop containing non-volatile solutes (salts, macromolecules, deforming or not deforming colloidal par-

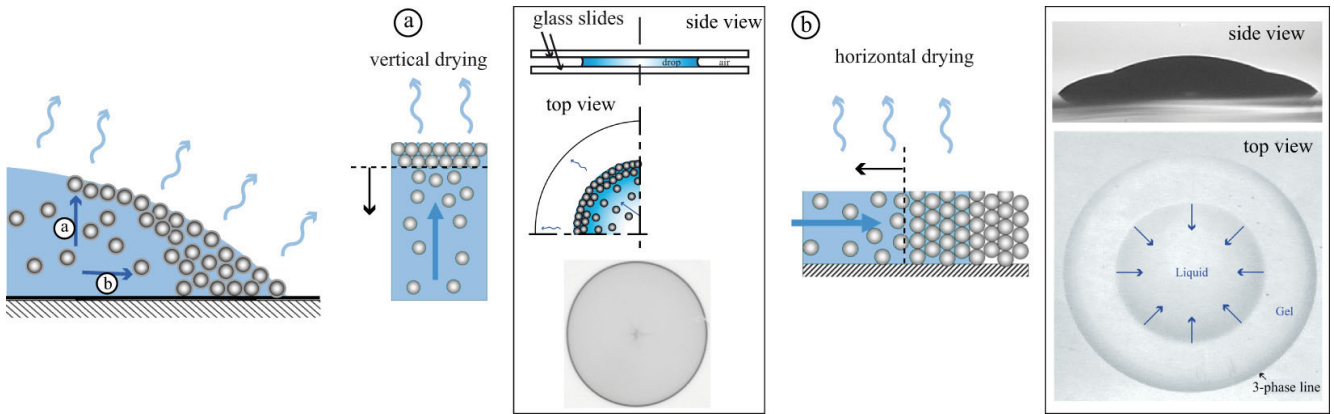


Fig. 8. Sketch of the colloidal array accumulated (a) at the drop surface and (b) at the edge of a sessile drop. The transport of solvent driving the particles at the drop surface can be followed by considering the case of a drop confined between two circular transparent plates as sketched in (a). The growing deposit at the drop edge can be followed by side and top view as sketched in (b). Figure adapted with permission from Eur. Phys. J. E [31] (Copyright (2014) EDP Sciences, Società Italiana di Fisica, Springer).

ticles, etc.), solidification induced by drying results in the propagation of a drying front. This front separates a fluid domain, governed by the Stokes regime, from a porous region, where the solvent flows through the particles network by permeation accordingly with the Darcy law. The drying front shape and evolution with time are of great importance in the formation of the dried solid; indeed, the drying front determines the accumulation and the distribution of the solutes in the final material. In the case of a sessile drop, the evolution of the drying front is complex since its local velocity is governed by the local evaporation rate. In particular, two main drying processes can be highlighted as shown in fig. 8. i) The drying starts at the drop surface and the drying front moves from top to bottom in the vertical direction: this is the vertical drying resulting to a solid envelope, *e.g.* skin, formation (fig. 8(a)). ii) The drying starts at the rim and the drying front moves horizontally: this is the so-called horizontal drying leading for example to solid drop edge (fig. 8(b)). In particular, for small contact angles, the horizontal drying is generally faster than the vertical one due to the high evaporation rate at the drop edge. The resulting radial outward flow of solvent is expected to generate solid regions that are thicker near the pinned contact line than the apex.

Different authors have treated the liquid-solid transition induced by drying, the vertical and the horizontal drying processes. The main considerations follow.

3.1 Transition liquid-solid

During the drying process, the increase of the non-volatile solutes concentration, ϕ , can be described by a non-linear advection-diffusion equation with a collective diffusion coefficient, $D_{coop}(\phi)$ [11, 32]:

$$\partial_t \phi + \nabla \cdot (\phi \vec{J}_s) = \nabla \cdot (D_{coop}(\phi) \nabla \phi). \quad (6)$$

Here the collective diffusion coefficient strongly depends on the concentration and captures the interaction between

the solutes on the solvent transport as well as the hydrodynamics interactions as previously shown by Russel *et al.* [33]. Upon concentration increase, the collective diffusion coefficient increases, accelerating the equilibration of concentration distributions via cooperative motion:

$$D_{coop}(\phi) = D_0 \frac{K(\phi)}{k_B T} V_p \frac{\partial \Pi}{\partial \phi}, \quad (7)$$

where D_0 is the Stoke-Einstein diffusion coefficient for dilute limit, $K(\phi)$ denotes the sedimentation coefficient that describes the hydrodynamic interactions at finite concentration, k_B is the Boltzmann constant, T is the absolute temperature, V_p the volume of the suspended solutes, and Π the osmotic pressure that expresses as

$$\Pi(\phi) = \frac{k_B T}{V_p} \phi Z(\phi) \quad (8)$$

with $Z(\phi)$ the osmotic compressibility of the solution accounting for the effect of solutes interaction on the osmotic pressure.

The simplest case to quantify the concentration gradient is a 2D configuration that uses a rectangular thin cell with a single evaporation surface [34]. This cell is made from two glass slides separated by spacers placed along both longest sides. During the drying, particles accumulate near the open surface. This geometry provides information in a modeled slice perpendicular to the evaporation surface of a drop. Concentration gradients were measured using Small-Angle X-rays Scattering (SAXS), and fluorescent dye or organic dye adsorbed by the colloidal particles (fig. 9(a)). The increase of the concentration of solutes is well described by the advection-diffusion equation (6). Moreover, SAXS provided structural information such as the appearance of an anisotropy generated by a uniaxial strain of the liquid dispersions as they are compressed by the flow of water toward a solidification front. This anisotropy was observed for a particle volume fraction equal to 0.35.

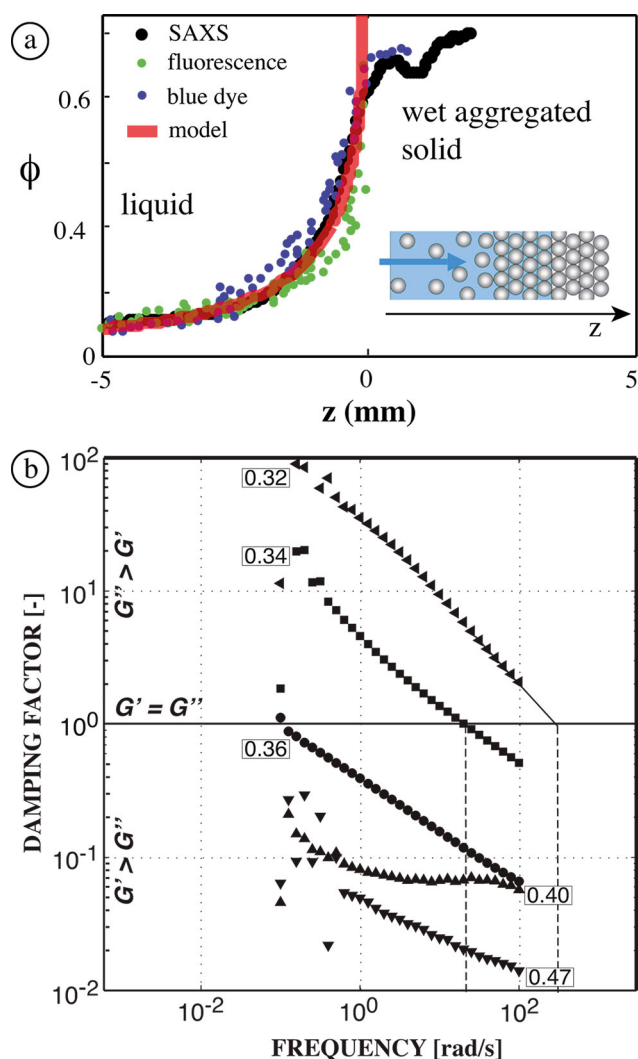


Fig. 9. (a) The increase in volume fraction (black points obtained using SAXS measurements; figure adapted with permission from [34] Copyright (2014)) is well described by the balance between advection along z , and diffusion back down concentration gradients (red curve). (b) Rheological behaviour for Ludox HS-40 colloidal dispersions with particles volume fraction ranging from 0.32 to 0.47 subjected to an increasing oscillatory strain (10^{-2} – $10^3\%$). The storage, G' , and loss, G'' , moduli are plotted as a function of frequency. The curve intersection with the line $G'' = G'$ gives the relaxation time of the samples (figure adapted with permission from Rheol. Acta [35] (Copyright (2012) Springer)).

In addition to this nanoscopic result, the concentration of solutes results in a variation of the rheological properties of the drying solution. These properties were investigated using rheometric measurements by oscillatory tests. As a result the storage, G' , and loss, G'' , moduli that characterize the stored elastic energy and the energy dissipated by heat respectively were measured as a function of strain. Di Giuseppe *et al.* [35] showed that samples with a concentration higher than 0.37 involve a growing elastic behaviour (fig. 9(b)). Thus, the change of rheological behaviour, G' and G'' , together with the build-up of an

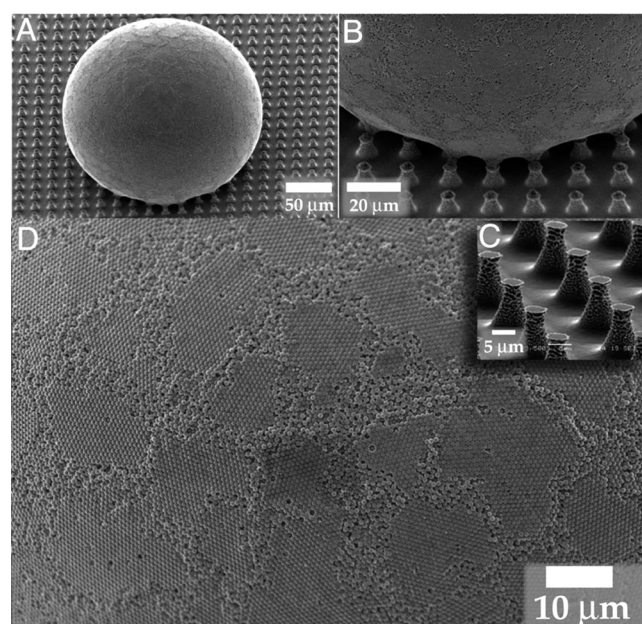


Fig. 10. (A) Tilted view of the supraball in contact with the microstructure. (B) Detail of the contact area. (C) Magnified view of the micropillars forming the microstructure. (D) Close-up of the supraball surface. The distribution of crystalline patches resemble the pentagons in a soccer ball. Reprinted figure from [36].

anisotropy at nanoscale support the build-up of a structure at the similar solutes concentration.

Finally, the shear rigidity of the drying solid also increases substantially as the non-volatile solutes approach close packing.

3.2 Vertical drying of sessile drops of solutes

In this section, the effect of a substrate is not considered and the mean flow of non-volatile solutes perpendicularly to the drop surface is considered. This process is a direct consequence of the so-called “vertical drying”. A flow induced by the evaporation rate advects the non-volatile solute towards the drop surface resulting in a spatial distribution. Using the drying colloidal dispersion droplets on superhydrophobic substrates, Marin *et al.* [36] investigated colloidal microstructures induced by radial flow. The authors showed that the number of particles and their packing fraction can be controlled in the microstructures (fig. 10).

The importance of the vertical drying depends on the advection and diffusion processes. Indeed, considering a densely packed region at the drop surface, says an “envelope”, that grows at a velocity w , the advection-diffusion length for non-interacting solutes is predicted to evolve as $D_0/(J_s - w)$ [34]. The influence of advection and diffusion in the formation of an envelope can be determined by a dimensionless number, the Péclet number in the vertical direction, Pe_V . The Péclet number compares the advection and diffusion characteristic times. In the case of a sessile drop, $Pe_V = J_s H_0 / D_0$, where H_0 is the apex height

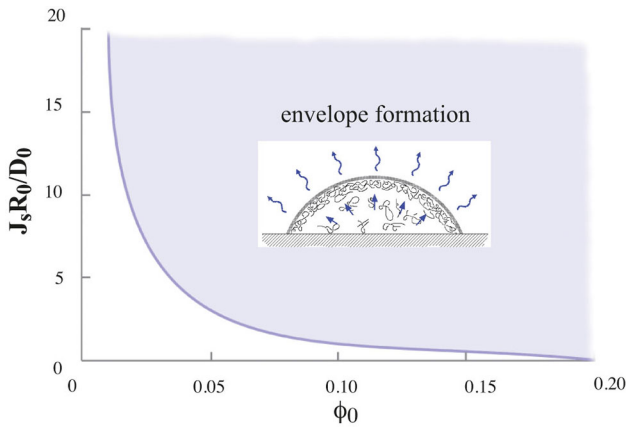


Fig. 11. Diagram of skin formation following the evaporation rate through the vertical Péclet number $Pe_V = J_s R_0 / D_0$, and the initial concentration in non-volatile solutes, ϕ_0 . Above the solid line, well-structured skin layers are formed. This plot was reconstructed from [11].

of the drop as a typical lengthscale, and D_0 the diffusion coefficient of the non-volatile solutes.

Indeed, when diffusion dominates ($Pe_V \ll 1$), the solutes distribution is predicted to remain uniform through the drop thickness as it dries. When evaporation is the dominant mechanism ($Pe_V \gg 1$), accumulation of solutes at the air-liquid interface takes place. The resulting skin, or crust, can be controlled by Pe_V and the initial volume fraction of the solution ϕ_0 by the criterion [11]: $Pe_V > \frac{\phi_g - \phi_0}{(1 - \phi_0)\phi_0}$, where ϕ_g is the volume fraction characteristic of the structure of the solid region. The evolution of volume fraction of colloidal particles was numerically obtained for various Péclet numbers by Routh *et al.* [37].

The wet solid region formed at the drop surface appears preferentially at high evaporation rate or high initial solutes concentration as shown in fig. 11. Moreover, the cohesion of this solid region is strongly affected by the interaction between the non-volatiles solutes and the presence of the ionic species. By the way, the formation of the wet solid region at the drop surface depends on the physicochemical conditions (controlling the interaction between the non-volatile solutes) and the way the non-volatile solutes accumulate at the free surface. For small contact angle, the vertical drying is generally slower than the horizontal one due to the high evaporation rate at the drop edge.

3.3 Horizontal drying of sessile drops of solutes

The horizontal drying results in the transport of particles laterally to the edges of a sessile drop, in the condition of a vertical Péclet number $Pe_V = 0$. The situation is a more complicated mainly due to the presence of the substrate and the resulting singularity at the contact line. This process has been largely studied since it partly governs the morphologies of final deposits on the substrate [38]. This self-pinning results in an outward flow that transport the non-volatile solutes toward the contact line and leads to the formation of a ring. For concentrated

fluids, the growing deposit is induced by the lateral transport of non-volatile solutes [39,40]. Winnik *et al.* proposed a drying process where the propagation of a lateral front was due to evaporation from a region at the edge where particles had concentrated to form a close packed structure [41]. Moreover, using a derivation of the equations governing the flow of evaporating films in the lubrication limit, Routh *et al.* [42] elaborated mathematical models to obtain the evolution of the horizontal propagation of the drying front due to continued evaporation from the packed region. Nassar *et al.* [43] have recently pointed out the different contributions causing this lateral transport: capillary flow at the drop edge, Laplace and Marangoni flow due to surface tension changes. The time evolution of the drying front was captured by a horizontal Péclet, Pe_H , defined as a function of the flux in the lateral direction, and the capillary length: $Pe_H = u_r l_c / D_{coop}$, where u_r is the fluid velocity in the lateral direction. In particular, the authors showed that the collective diffusion slows down the drying front [43].

The large variety of patterns left on a surface by the drying drops ranges from the ring-shaped deposit of particles around the edge of the droplet, multiple rings, stripes, spikes, and fractal-like lace to uniformly distributed solutes [44–46]. Two types of patterns are shown in fig. 12. The multiplicity of deposits depend on various parameters: of these are the nature and the concentration of the solutes, the interaction between solutes and between solutes and the substrate, the solutes shape and polydispersity, . . . Moreover, the contact line behaviour where the deposition takes place is mainly responsible for this variety of morphologies.

In general, the contact line of the drop is pinned due to a rapid deposition and adhesion of the solutes on the substrate at the drop edge. Then the contact line can move remaining pinned at the same position during a more or less long time, resulting in successive rings whose number particularly increases with non-volatile solutes concentration. The key factors controlling the “stick-slip” mechanism are: evaporation rate that is significantly controlled by the contact angle, the surface interaction between solutes and substrate (a non-perfect substrate can be at the origin of the stick-slip pattern). Such a stick-slip pattern is shown in fig. 12(a). On the contrary, strong pinning results in a coffee-ring formation as shown experimentally in fig. 12(b) and numerically in fig. 12(c).

A structural transition in the stain was investigated by Marin *et al.* [47] using monodisperse colloidal particles. Since an ordered phase is observed by the particles arriving early at the contact line, those arriving during a rush hour, at high deposition rates, form a disordered phase (fig. 12(d)). This effect was related by the authors to the popular *Tetris* game since slowly falling objects are easily packing in regular structures, while faster falling objects become disordered.

In the case of polydisperse particles, a segregation at the edge of a sessile drop was also studied. This was investigated in mixtures of micrometric and nanometric particles as shown in fig. 12(e) [48]. Fingering pattern in the

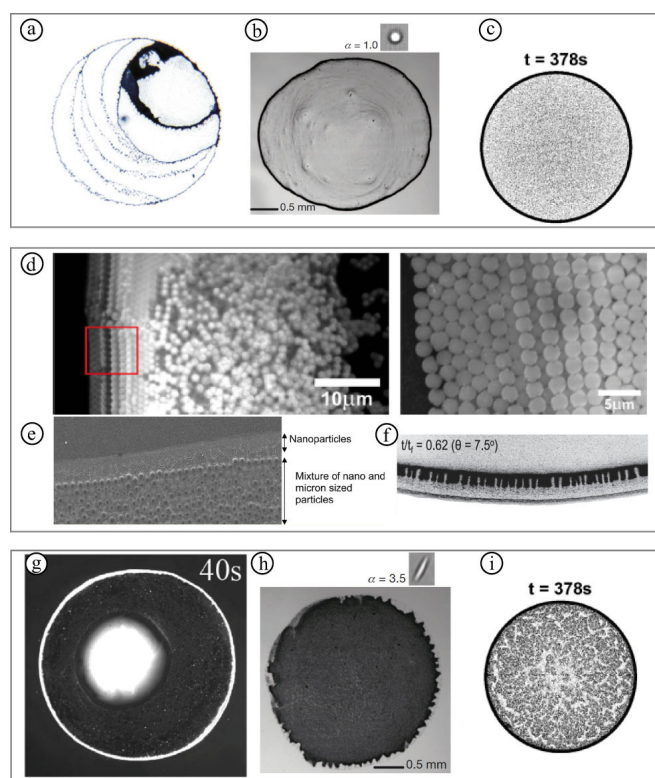


Fig. 12. Desiccation patterns of sessile drops of nanofluids. (a) Multi-ring patterns in the suspension of titanium dioxide nanoparticles in ethanol following a “stick-slip” regime. Reprinted with permission from [49] (Copyright (2009) American Chemical Society). (b) Coffee-ring formation in a water drop containing a suspension of micro-sized polystyrene spheres. Inset, particle shape. Adapted with permission from Nature [50] (Copyright (2011) Springer, Nature). (c) Ring-shaped deposition formed by microspheres (numerical simulation); Reprinted with permission from [51] (Copyright (2017)). (d) Order-to-disorder transition in the particle stain left by an evaporating drop. Reprinted with permission from [47] (Copyright (2011) American Physical Society). (e) Segregation: nanometric colloids segregate at the edge of a sessile drop, whereas micrometric colloids are blocked further away from the edge. Reprinted with permission from [48] (Copyright (2011) American Chemical Society). (f) Fingering in the stain resulting in a bidispersed colloidal mixture of micro and nanoparticles. Adapted with permission from [52] (Copyright (2013) American Physical Society). (g) Effect of the substrate temperature. In a water droplet containing PS spheres, a central stain gradually appears by increasing the substrate temperature. As a result a central stain gradually appears. Adapted from [53] with permission of The Royal Society of Chemistry. (h) Effect of the particle shape: suppression of the coffee-ring effect by shape-dependent capillary interactions in the case of a water drop containing a suspension of anisotropic particles. Inset, particle shape. Adapted with permission from Nature [50] (Copyright (2011) Springer, Nature). (i) Effect of the particles interaction: uniform deposition using a mixture of spherical and non-spherical particles with enhanced particle-particle interaction at air-water interface (numerical simulation). Reprinted with permission from [51] (Copyright (2017)).

stain was also observed as a result of a bidispersed colloidal mixture of micro- and nanoparticles. The finger formation is driven by competition between the coffee-ring and Marangoni effects as shown in fig. 12(f) [52].

Besides, several studies have been devoted to control and/or eliminate or reverse the coffee stain for the last past decade. Some methods to control the morphologies of deposits follow. The Marangoni flow direction strongly affects the solutes transport in the drying drop and by the way the final morphologies of the deposits. That is why several studies have taken advantage of the Marangoni flows to limit and possibly reverse the coffee stain. Among them, the thermal Marangoni flow was theoretically and experimentally investigated in ref. [54]. Heating the substrate creates a gradient in surface tension inducing an inward Marangoni flow from the hot region (the drop periphery) toward the cool one (the drop apex) (fig. 12(g)) [53].

The effect of the particle shapes (spheres, platelets and tubes) also affect the formation of stains. The presence of anisotropic particles significantly deforms interfaces, producing strong interparticle capillary interactions. This effect acts as a ring inhibitor as shown in fig. 12(h) as opposed to the ring formation with spherical particles (fig. 12(b)) by the same authors [50]. Moreover, the effect of non-spherical particles in the suppression of the coffee ring was also investigated using Discrete Element Model as shown in fig. 12(i) as opposed to the stain formation with spherical particles (fig. 12(c)) by the same authors [51].

Another method to inhibit the stain involves a physicochemical modification of the fluids to tune the viscosity, the surface tension, the interaction between solutes, or the evaporation rate of the solvent. Particularly, the addition of surfactant-like viscous polymer to support centripetal Marangoni flow [55], or tuning colloid-polymer interactions inhibit the coffee stain [56,57], or else binary mixture made of a small concentration of surfactant and surface-adsorbed polymer which offers a physicochemical avenue for control of coatings [58]. Without modification of the physicochemical properties of the fluids, acoustic waves have been recently investigated to control the solutes transport and eliminate the coffee stains [59].

4 Mechanical instability

During the solvent loss, the non-volatile compounds accumulate near the vapour/drop interface. A solid region builds up over this surface. The mechanical properties of this region depend on the physicochemical properties of the solutes, also on the drying kinetics that is controlled through the humidity rate, RH . A consequence can be the build-up of high mechanical stress caused by high capillary pressure in the close-packed of solutes. The stress release leads to the occurrence of instabilities. A skin at the drop surface may buckle under the effect of mechanical instabilities, or a structure at the drop edge can fracture. The following section is devoted to give some aspect of these mechanical instabilities, and point out the resulting morphologies.

4.1 Buckling instabilities

During solvent removal of drops of solutes, the outer layer of the drop exhibits a high non-volatile solutes concentration. The solvent evaporation leaves a solutes-concentrated region near the drop surface. This concentrated region is then regarded as a skin or a crust, or more generally as an envelope. When the structural strength of this region is sufficient, the envelope can withstand internal stress. Then buckling process induced by the drying is a way to release the drying stress. As an example, different behaviours can be observed during the drying of quasi-spheroidal colloidal drops deposited on superhydrophobic surface (see fig. 13) [13]. For high initial concentration, the drop behaves initially like pure liquid drop, then shrinks isotropically while the envelope thickens up to a critical value. Then the thick envelope resists to the drying stress preventing further distortions (fig. 13(a)). For a low initial concentration of the dispersion, an elastic envelope shrinks then buckles as a result of the decrease of the inner volume: an inversion of curvature occurs as shown in fig. 13(b). Experimentally the concentration gradient of non-volatile solutes at the drop surface, the resulting envelope formation and distortion can be investigated using an appropriate geometry: a drop sandwiched between two parallel circular glass slides whose gap is controlled [60] (fig. 13(c)). In this quasi-2D geometry, the evaporation flux is radial and drives the accumulation of non-volatile species at the liquid/air interface [8, 61, 62]. In this case, the resulting single depression grows and is continued by an invagination tube penetrating inside the drop.

In the case of non-deforming colloidal particles, a dense assembly progressively forms and results in the formation of a porous shell. As the shell thickness increases, the close-packed nature of the particles at the drop surface encloses a liquid phase that permeates through it during the drying. The evaporation can be progressively blocked in the case of deforming colloidal particles that deform as a result of high capillary pressure at the evaporation surface.

In general, the mechanical properties of the envelope evolve with time, and exhibit viscoelastic, elastic, or elastoplastic behaviours that strongly depends on the physicochemical properties of the solutes. The mechanical properties of the envelope can be tuned by modifying the ionic strength or adding a polymer [63, 13, 14]. A great interest to control the mechanical properties of the envelope is that the distortion of drops is determined by them. This is particularly the case for spray drying in which the shape of the final drop is not determined by the Péclet number, whose value remains far larger than unity in usual conditions, but depends on the mechanical properties of the envelope [64].

The onset of buckling and the different distortions of drops dried at room temperatures generally depend on the mechanical properties of the envelope, also the drying kinetics. Different morphologies are presented in fig. 14 for various initial contact angle of the drop on the substrate, and for different humidity rate governing the drying kinetics [65, 12]. The diagram was investigated through drying

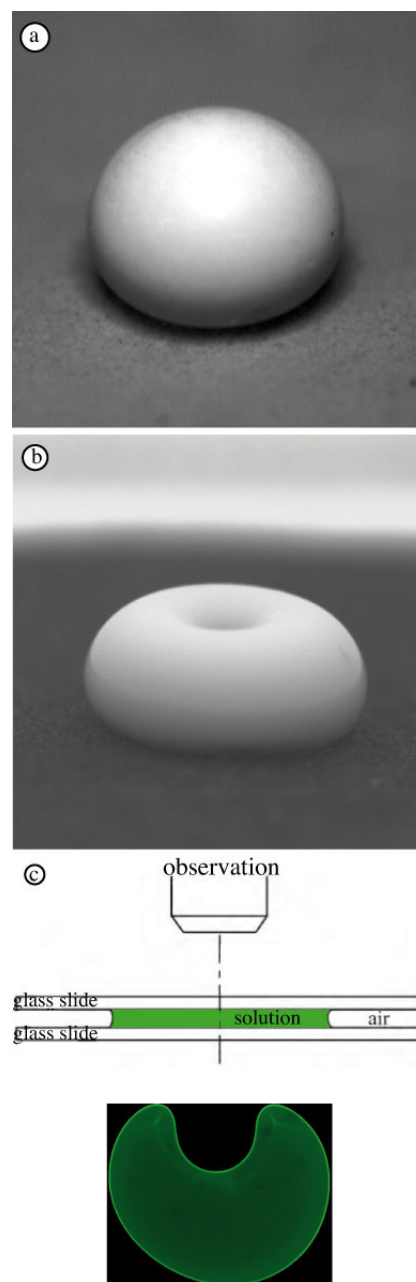


Fig. 13. Digitized images of colloidal droplets deposited on super-hydrophobic surfaces at the final stage of desiccation (the drops meridian radii are 1.2 mm). The photographs show 2 shapes obtained for different values of the initial particle volume fraction in the same drying conditions. (a) At large particles concentration, the shrinkage is uniform. Figure adapted with permission from [13] Copyright (2004). (b) At low particle concentration, an elastic envelope forms at the evaporation surface; as the inner volume is reduced due to evaporation, a local buckling of the envelope occurs at the top of the drop. The distortion together with the envelope thickness can be observed during the drying using a confined drop as a slice of the 3D drop (c): a droplet of solution is sandwiched between two circular glass slides (sketch in side view). The gap between both glass slides is controlled by spacers; the thin cell is illuminated by transmitted light.

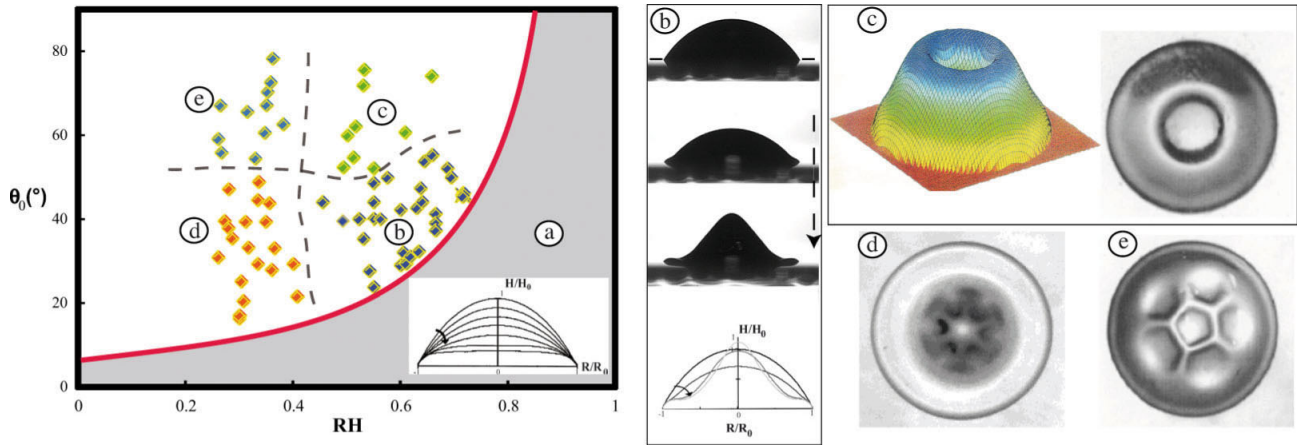


Fig. 14. Diagram showing the different behaviors displayed by sessile drops following the initial contact angle (θ_0) and the humidity rate (RH). For small contact angle and relatively large RH , drops regularly flattens as shown by the superposition of profiles (region (a) in gray). This region is limited from unstable evolutions by the red line in agreement with the theoretical predictions. Different unstable evolutions are observed and result in 4 main domains. Region (b): the drop keeps its axisymmetry and distortions result in a buckling instability (profiles evolutions in (b) —reprinted figure with permission from [12] (Copyright (2013))). Region (c): the drop forms a dip at its center (3D map measured using a mechanical profilometer in (c) [66]). Region (d): a peak first forms at the drop center, and later radial wrinkles build-up, breaking the axisymmetry (top view in (d) —reproduced from [67]. (Copyright (2003) Elsevier Masson SAS. All rights reserved.)) Region (e): a complex pattern progressively builds up involving a cascade of buckling (top view in (e) —reproduced from [67]. (Copyright (2003) Elsevier Masson SAS. All rights reserved.)) Each drop base diameter is 4 mm; the dotted line in the first image in (a) corresponds to the drop/substrate contact.

sessile drops of a water-soluble polymer that undergo the glass transition at room temperature, so leading to the formation of a polymer outer skin in the glassy state. The contact base of the drop remains constant during the drying process as a result of the concentrated drop solutions.

For low contact angles and high humidity rate, the envelope at the drop surface is not well defined in comparison with the bulk. Consequently, the drop progressively flattens: the drop shape is not strongly modified and its apex height regularly decreases (region (a) in fig. 14). On the contrary for larger contact angles and lower humidity rates, the envelope undergoes mechanical instabilities whose occurrence was studied in refs. [65, 12]. Indeed, the shell buckles under the decrease of the volume that it encloses while its surface area remains constant (fig. 14(b)). For a large contact angle, the shape change results in the formation of the circular fold as shown in fig. 14(c) [65, 68]. Under high humidity rate, thin elastic envelopes display a complex pattern progressively builds up involving a cascade of buckling: a breaking of the drop axisymmetry can occur for elastic envelope leading to the formation of radial wrinkles (fig. 14(d), (e)): the number of these wrinkles increases when the thickness of the shell decreases. The final drop shape can also display a circular fold as shown in fig. 14(c). These shape instabilities were investigated in the case of polymer solutions as well as dispersions of nanometric particles under controlled physicochemical properties.

Simulation and scaling analysis were investigated to model the deformation mode and stability properties of elastic caps with a non-uniform thickness profile [69]. The onset of the buckling was precisely quantified in the case of freely-suspended colloidal drops using Leidenfrost effect [14].

Moreover, simple considerations to point out the unstable behaviors are based on two timescales that govern the evolution of sessile drops: the drying timescale t_E , that is the time needed for water drops to dry completely, and the time, $t_{envelope}$, that is needed to form a solid envelope at the drop surface [65, 12]. Using eq. (2), where the drop size is chosen as the radius of the contact base of the drop, and $4, t_E$ expresses as

$$t_E = \frac{R_0}{J_s} = f(\theta_0, RH)R_0^2, \quad (9)$$

where f is a function given in [65]¹.

$t_{envelope}$ is quantified by considering the transfers inside the solution. As evaporation proceeds, the polymer concentration at the vapour/drop surface increases. Solvent flux conservation at air drop interface writes: $J_s = D_m \nabla \phi_p$, where D_m is the mutual diffusion coefficient and ϕ_p is the local value of the polymer volume fraction. In order of magnitude, the concentration gradient $\nabla \phi_p$ is the ratio between the variation of concentration of non-volatile solutes in the core of the drop and the vapour/drop surface on the typical diffusion length $\sqrt{D_m t}$. Thus $t_{envelope}$ is expressed as:

$$t_{envelope} = g(\theta_0, RH)R_0^2 \quad (10)$$

where g is a function given in [65]².

¹ $f(\theta_0, RH) = \frac{1}{D_{vap}} \frac{1}{A(\theta_0)} \frac{n_l}{n_{vs}} \frac{1}{1-RH}$, where $A(\theta_0)$ is a numerical factor related to the shape of the isoconcentration curves of water in accordance with ref. [65].

² $g(\theta_0, RH) = \frac{D_m (\phi_{pg} - \phi_{p0})^2}{D_{vap}^2} \left(\frac{n_l}{n_{vs}}\right)^2 \frac{1}{A(\theta_0)^2} \frac{1}{(1-RH)^2}$, where $A(\theta_0)$ is a numerical factor related to the shape of the isoconcentration curves of water in accordance with ref. [65].

Therefore, if $t_E < t_{envelope}$ the drop flattens progressively due to solvent evaporation (fig. 14(a)). The desiccation is very fast and is too fast for the core of the sessile drop to be still fluid when a glassy or gelled envelope forms at the drop surface; this is the typical behaviours of sessile drops with low contact angles.

If $t_E > t_{envelope}$ there is enough time for an elastic envelope to build-up at the drop surface before complete desiccation and instability take place during drying (unstable behaviours in fig. 14). Comparing these two characteristic times suggests a criterion for the occurrence of the instability. The limit of the instability domain given by $t_E = t_{envelope}$ is in agreement with the experimental results on drops of polymer solutions (fig. 14).

4.2 Cracking

Another way to release mechanical stresses is to nucleate and propagate cracks [70,71]. In this way, drying cracks are usually observed in drops of toothpaste left to dry on a sink, a droplet of blood, or in mud puddles. In particular drying cracks in growing drop stains are studied since the sessile drop is a geometry that naturally induces a thickness gradient providing directional cracks growth [72, 73]. Drop stain usually exhibits porous network filled with solvent, or gel phase, in which drying stress build up as a result of the pressure gradient in the pore liquid. In particular, the capacity of a gel network to crack during drying depends on the existence and significance of a pressure gradient in the pore liquid and the way the gel relaxes the induced drying stress [74]. Quantifying drying stress requires a theory coupling fluid dynamics and solid mechanics. Indeed, in the gel phase, the spatial and time variations of the pressure, p , in the liquid pores satisfies [75]:

$$\frac{\partial p}{\partial t} = D_p \frac{\partial^2 p}{\partial z^2}, \quad (11)$$

where $D_p = \frac{kE_p}{\eta}$ is the diffusivity, also called consolidation coefficient, E_p being the elastic modulus of the gel, k the permeability of the porous gel, and η the solvent viscosity.

Equation (11) together with the boundary condition at the upper surface of the film: $\frac{\partial p}{\partial z}|_{free\ surface} = -\frac{J_s \eta}{k}$ give both spatial and time variations of the pore pressure $p(z, t)$ [31]. Considering the gel initially uniform without pressure gradient ($p(z, t = 0) = p_0$), the stress $\sigma_{i,j}$ in the plane of the film expresses as

$$\sigma_{i,j}(z, t) \propto p_0 - p(z, t) \quad (12)$$

where the subscripts i, j refer to the polar coordinates whose origin is the centre of the drop. Equations (11) and (12) show that the drying stress averaged over the gel thickness linearly increases with time [31]:

$$\overline{\sigma_{i,j}(t)} \approx E_p \frac{t}{t_E}. \quad (13)$$

The stress build-up in the porous film notably depends on the particles (size, rigidity [76], and interaction between

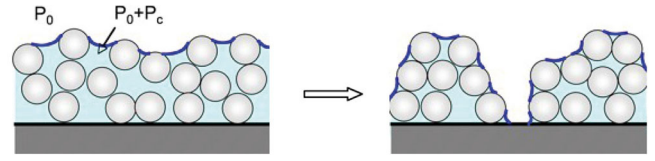


Fig. 15. Mechanism responsible for crack formation: capillary forces exert a compressive stress on the surface layer of the porous film.

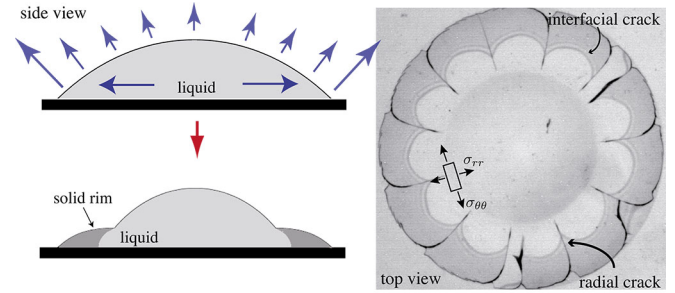


Fig. 16. (Left) Sketch of a drying sessile drop in side view. During evaporation, the periphery of the drop is solid while the central part is liquid. (Right) Pattern of radial cracks formed all around the sessile drop periphery while the central part is liquid. The well-defined crack spacing is related to the maximum value of the solid gel thickness at time the crack form; this pattern was studied in ref. [31]. The dark region is due to an interfacial crack between the gel and the substrate—silica dispersion of Ludox HS-40, base diameter 4 mm and $RH = 50\%$ [77].

them affecting the elastic modulus), the way the particles structure the wet gel (drying kinetics), and the drop size captured in the drying timescale t_E (eq. (9)).

In particular, the maximum liquid pressure that can be supported by an array of particles is determined by the solvent/air surface tension. For monodisperse particles, at random close packing, the capillary pressure is determined as $5.3\gamma/a$, a being a particle size [74]. As soon as the medium solidifies, this pressure creates a contractive stress on the surface gel (fig. 15). This is opposed by the adhesion of the drop on the substrate, which does not contract. The resulting stress is possibly released by the formation of cracks. In the geometry of a sessile drop exhibiting small contact angle, the main components of the mechanical stress field in the growing solid rim are radial, σ_{rr} , and ortho-radial, $\sigma_{\theta\theta}$ (fig. 16 (right)). Geometric considerations showed that ortho-radial stress is preferentially released by propagating radial cracks. Figure 16 shows an image of the well-defined spatial organization of radial cracks in the solid rim [31].

Generally, crack patterns depend on the network resistance, the drop geometry, and drying conditions. Moreover, crack spacing in films increases with the film thickness. The same variation holds in the case of the radial crack spacing in sessile drops. Indeed, in drying sessile drops the average height of the rim depends on the contact angle. This last can be modified by changing the surface energy of the substrate. Thus, the mean radial crack

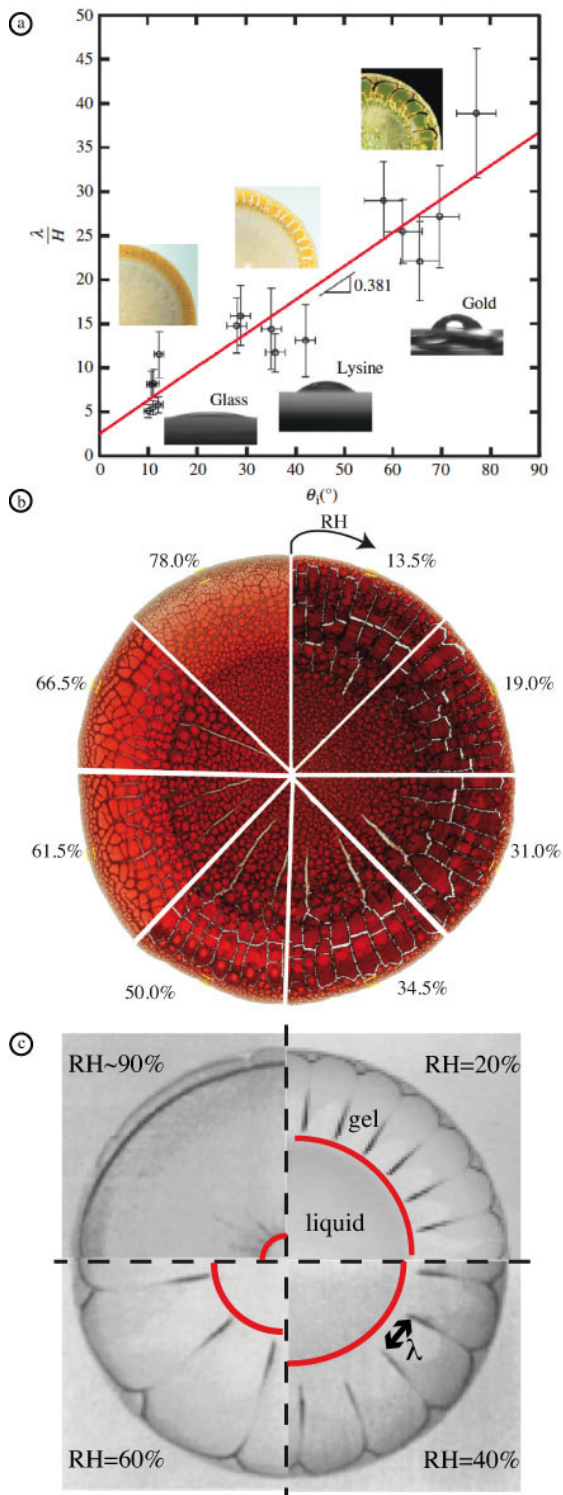


Fig. 17. (a) Dimensionless mean radial crack spacing as a function of the contact angle of the drop on the surface. Reprinted with permission from [78] (Copyright (2013) American Chemical Society). (b) Morphologies of cracks in drying sessile drop of blood for various humidity rates RH . Reprinted with permission from [79] (Copyright (2013) Elsevier). (c) Similar influence of the humidity rate on the crack pattern in sessile drops of a silica dispersion (base diameter 4 mm). The wavelength was experimentally studied for various drying rate and contact angle of the drop on substrates in ref. [31].

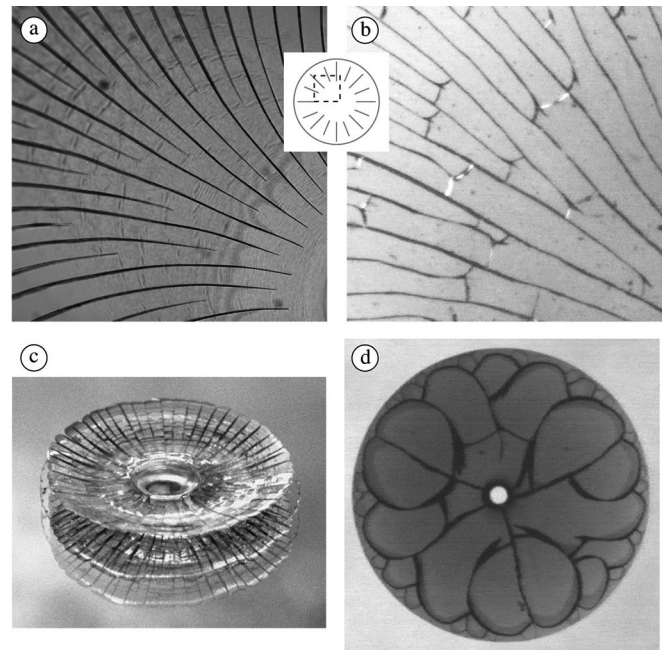


Fig. 18. Various crack organisations in drying sessile drops of colloidal dispersions. (a), (b) The cracks, as they grow, are forced to be nearer to each other than needed, to release the stress (see sketch of the radial cracks in a drop in top view). Some cracks stop growing (a) or connect perpendicularly to their neighbours (b). (c), (d) The final crack pattern in sessile drops of two different colloidal dispersions (drop diameters: 3 mm): (c) once the radial crack reach the center of the sessile drop, the petal-shaped fragment possibly delaminate and bend under differential stress (dispersion of silica particles) reprinted with permission from Eur. Phys. J. E [31] (Copyright (2014) EDP Sciences, Società Italiana di Fisica, Springer); (d) disorder crack pattern formed after the whole sessile drop solidifies.

spacing was plotted as a function of the contact angle in fig. 17(a) [79,80].

Moreover, crack patterns strongly depend on the drying conditions [31]. Figure 17(b) shows typical crack patterns in the blood drops dried at different relative humidities RH ; the same variation was investigated in drops of nanoparticles. The number of radial cracks increases when RH is decreased. Indeed, the stress build-up is affected by the drying kinetics accordingly with eq. (13). Moreover, the internal structure is probably modified by the drying kinetics.

The geometry of a sessile drop naturally involves centripetal solidification and thickness gradient. In this way, this is a well-adapted geometry to investigate the interaction between cracks that depends on the mechanical properties of the dried gel. As an example such crack interaction is shown in fig. 18(a), (b) when radial cracks approach the drop centre. Generally crack network exhibit various morphologies which depend on the mechanical properties of the system. Delamination of petal-shaped fragments in a dried drop of silica nanoparticles (fig. 18(c)) or disordered channelling crack pattern in a dried drop of latex nanoparticles (fig. 18(d)).

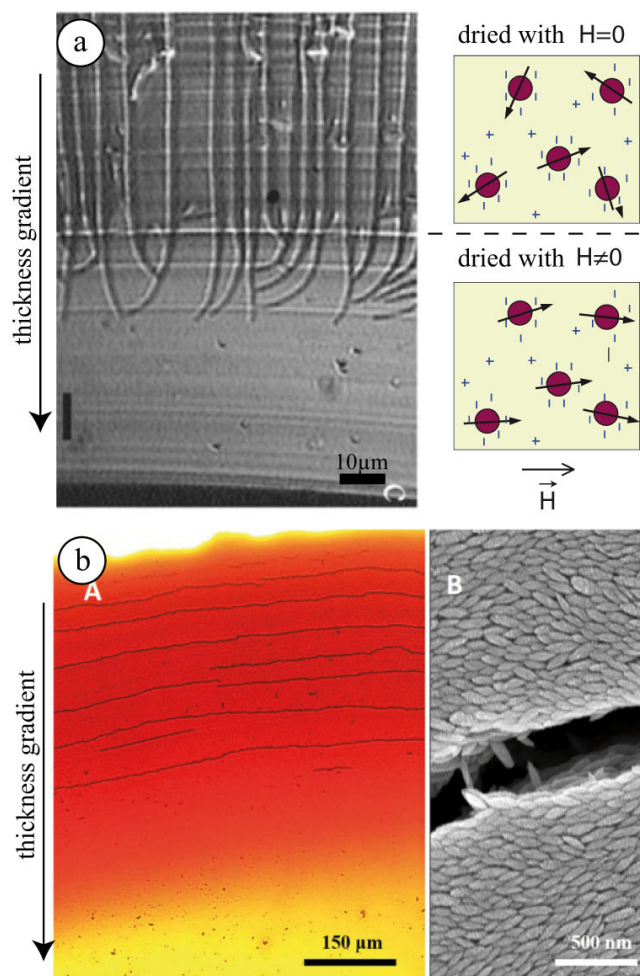


Fig. 19. (a) Initially, the propagation of the array of parallel cracks is induced by the directional drying; when entry the region dried under an oriented magnetic field, H , cracks change their trajectories to satisfy the anisotropy of the colloidal gel dried under the magnetic field. Sketch of an ionic ferrofluid. In the absence of an applied magnetic field, the magnetic moments of the particles are randomly oriented because of the Brownian motion, whereas they are aligned under the effect of an applied magnetic field (reprinted with permission from [81] (Copyright (2008) American Physical Society)). (b) Cracks are formed along the radial direction for spherical particle dispersions whereas circular crack paths are formed with ellipsoidal particle dispersions; figure reprinted with permission from [82] (Copyright (2016) Nature Publishing Group).

Controlling the crack path is very important in various situations. Inversely, the morphology of cracks is a way to reveal some mechanical properties of the solid matter. The drying of sessile drops of spherical nanoparticles leads to cracks propagating radially from the drop edge as the gel phase extends from the periphery to the centre of the drop. This is the most common behaviour. The same pattern is observed during the drying of a sessile drop of ferrofluid in which the nanoparticles carry a permanent magnetic moment (see the sketch in fig. 19(a)). However, in the presence of an external magnetic field, the magnetic moments of the particles tend to be aligned in the

same direction as the external field. It is then possible to change the trajectory of cracks by applying external magnetic field perpendicularly to the direction of propagation of the cracks as shown in fig. 19(a) [81]. The self-assembly of anisotropic particles can also result in changing a crack pattern (fig. 19(b)) [82]. In this case, instead of being aligned with the thickness gradient, cracks exhibit circular paths.

5 Conclusion

Drying droplets involve numerous physical processes from solvent diffusion to transfers at the vapor/medium interface. These processes result in solutes transport and their possible concentration at vapor/medium interface and the three-phase line. In this way, many works have concerned deposited nanoparticles and their ability to assembly. The drying kinetics, the physicochemical properties of the solutions and the role of the substrate have been shown to be key parameters to tune morphologies of the deposits. Since the observation and the understanding of the coffee stain, recent advances have raised the control of the physical processes responsible for the stain, then to eliminate or inverse the coffee stain. Moreover a significant part of this work has pointed out that the final deposits are usually affected by high mechanical stress that build up during the drying. Despite its complex geometry, a sessile drop can display astonishing regular patterns that are the signature of the material and the solidification dynamics. Indeed, the resulting mechanical instabilities such as cracks, debonding or wrinkles act as defects that affect the final film quality at a mesoscopic scale. An attractive perspective is the role of the substrate that exhibits a strong influence of the stress release and the morphologies of the deposits. In this way the surface energy and the rheological properties of the substrate could delay the occurrence of the mechanical instability and could tune the resulting dried pattern.

Author contribution statement

All the authors were involved in the preparation of the manuscript. All the authors have read and approved the final manuscript.

References

1. S. Kentish, M. Davidson, H. Hassan, C. Bloore, *Chem. Eng. Sci.* **60**, 635 (2005).
2. S.X. Qi Lin, X.D. Chen, *Technology* **27**, 1028 (2009).
3. C.S. Handscomb, M. Kraft, *Chem. Eng. Sci.* **65**, 713 (2010).
4. B. Sobac, D. Brutin, *Phys. Rev. E* **84**, 011603 (2011).
5. D. Attinger, C. Moore, A.D.A. Jafari, H.A. Stone, *Forensic Sci. Int.* **231**, 375 (2013).
6. J. Leng, *Phys. Rev. E* **82**, 021405 (2010).
7. L. Pauchard, M. Mermet-Guyennet, F. Giorgiutti-Dauphiné, *Chem. Eng. Process.* **94**, 483 (2011).

8. F. Giorgiutti-Dauphiné, L. Pauchard, J. Colloid Interface Sci., Suppl. C **395**, 263 (2013).
9. H. Hu, R.G. Larson, Langmuir **21**, 3963 (2005).
10. H. Wang, Z. Brutin, L. Huang, A. Mitra, Y. Yan, Langmuir **17**, 2572 (2001).
11. T. Okuzono, K. Ozawa, M. Doi, Phys. Rev. Lett. **97**, 136103 (2006).
12. L. Pauchard, C. Allain, Europhys. Lett. **62**, 897 (2003).
13. L. Pauchard, Y. Couder, Europhys. Lett. **66**, 667 (2004).
14. N. Tsapis, E. Dufresne, S. Sinha, C. Riera, J. Hutchinson, L. Mahadevan, D. Weitz, Phys. Rev. Lett. **94**, 018302 (2005).
15. C. Sadek, H. Tabuteau, P. Schuck, Y. Fallourd, N. Pradeau, C. Le Floch-Fouere, R. Jeantet, Langmuir **29**, 15606 (2013).
16. C. Sadek, P. Schuck, Y. Fallourd, N. Pradeau, C. Le Floch-Fouere, R. Jeantet, Dairy Sci. Technol. **95**, 771 (2015).
17. J. Maxwell, *Diffusion, Collected Scientific Papers* (Encyclopaedia Britannica, Cambridge, 1877).
18. B. Sobac, P. Talbot, B. Haut, A. Rednikov, P. Colinet, J. Colloid Interface Sci., Suppl. C **438**, 306 (2015).
19. B. Sobac, D. Brutin, Langmuir **27**, 14999 (2011).
20. R.D. Deegan, O. Bakajin, T.F. Dupont, G. Huber, S.R. Nagel, T.A. Witten, Phys. Rev. E **62**, 756 (2000).
21. B. Sobac, D. Brutin, in *Droplet Wetting and Evaporation*, edited by D. Brutin (Academic Press, Oxford, 2015) Chapt. 8: "Pure diffusion", pp. 103–114.
22. B.-J. de Gans, U.S. Schubert, Langmuir **20**, 7789 (2004).
23. J. Park, J. Moon, Langmuir **22**, 3506 (2006).
24. V.N. Truskett, K.J. Stebe, Langmuir **19**, 8271 (2003).
25. T. Kajiyama, W. Kobayashi, T. Okuzono, M. Doi, J. Phys. Chem. B **113**, 15460 (2009).
26. T. Still, P. Yunker, A. Yodh, Langmuir **28**, 4984 (2012).
27. Y. Tsoumpas, S. Dehaeck, A. Rednikov, P. Colinet, Langmuir **31**, 3334 (2015).
28. X. Xu, J. Luo, Appl. Phys. Lett. **91**, 124102 (2007).
29. H. Hu, R.G. Larson, J. Phys. Chem. B **110**, 7090 (2006).
30. H. Ishizuka, J. Fukai, Exp. Fluids **59**, 4 (2017).
31. F. Giorgiutti-Dauphiné, L. Pauchard, Eur. Phys. J. E **37**, 39 (2014).
32. R. Style, S. Peppin, Proc. R. Soc. London, Ser. A **467**, 174 (2011).
33. W.B. Russel, D.A. Saville, W.R. Schowalter, *Colloidal Dispersions* (Cambridge University Press, 1989).
34. F. Boulogne, L. Pauchard, F. Giorgiutti-Dauphiné, R. Botet, R. Schweins, M. Sztucki, J. Li, B. Cabane, L. Goehring, EPL **105**, 38005 (2014).
35. E.D. Giuseppe, A. Davaille, E. Mittelstaedt, M. François, Rheol. Acta **51**, 451 (2012).
36. Á. G. Marín, H. Gelderblom, A. Susarrey-Arce, A. van Houselt, L. Lefferts, J.G.E. Gardeniers, D. Lohse, J.H. Snoeijer, Proc. Natl. Acad. Sci. **109**, 16455 (2012).
37. A. Routh, W. Zimmerman, Chem. Eng. Sci. **59**, 2961 (2004).
38. R.D. Deegan, O. Bakajin, T.F. Dupont, G. Huber, S.R. Nagel, T.A. Witten, Nature **389**, 827 (1997).
39. S.G. Croll, J. Coat. Technol. **58**, 41 (1986).
40. Y. Ma, H.T. Davis, L.E. Scriven, Prog. Org. Coat. **52**, 46 (2005).
41. M.A. Winnik, J. Feng, J. Coat. Technol. **68**, 39 (1996).
42. A.F. Routh, W. Russel, AIChE J. **44**, 2088 (1998).
43. M. Nassar, A. Gromer, F. Thalmann, P. Hébraud, Y. Holl, J. Colloid Interface Sci., Suppl. C **511**, 424 (2018).
44. T. Yakhno, V. Yakhno, A. Sanin, O. Sanina, A. Pe-lyushenko, N. Egorova, I. Terentiev, S. Smetanina, O. Korochkina, E. Yashukova, IEEE Eng. Med. Biol. Mag. **24**, 104 (2005).
45. O. Goto, S. Tomiya, Y. Murakami, A. Shinozaki, A. Toda, J. Kasahara, D. Hobara, Adv. Mater. **24**, 1117 (2012).
46. M.D. Choudhury, T. Dutta, S. Tarafdar, Colloids Surf. A **432**, 110 (2013) (Wetting and evaporation: droplets of pure and complex fluids).
47. A.G. Marín, H. Gelderblom, D. Lohse, J.H. Snoeijer, Phys. Rev. Lett. **107**, 085502 (2011).
48. C. Monteux, F. Lequeux, Langmuir **27**, 2917 (2011).
49. J.R. Moffat, K. Sefiane, M.E.R. Shanahan, J. Phys. Chem. B **113**, 8860 (2009).
50. P.J. Yunker, T. Still, M.A. Lohr, A.G. Yodh, Nature **476**, 308 (2011).
51. T. Xu, M.L. Lam, T.-H. Chen, Sci. Rep. **7**, 42817 (2017).
52. B.M. Weon, J.H. Je, Phys. Rev. E **87**, 013003 (2013).
53. Y. Li, C. Lv, Z. Li, D. Quere, Q. Zheng, Soft Matter **11**, 4669 (2015).
54. W.D. Ristenpart, P.G. Kim, C. Domingues, J. Wan, H.A. Stone, Phys. Rev. Lett. **99**, 234502 (2007).
55. C. Seo, D. Jang, J. Chae, S. Shin, Sci. Rep. **7**, 500 (2017).
56. S.-a. Ryu, J.Y. Kim, S.Y. Kim, B.M. Weon, Sci. Rep. **7**, 1079 (2017).
57. Y. Ooi, I. Hanasaki, D. Mizumura, Y. Matsuda, Sci. Technol. Adv. Mater. **18**, 316 (2017).
58. H. Kim, F. Boulogne, E. Um, I. Jacobi, E. Button, H.A. Stone, Phys. Rev. Lett. **116**, 124501 (2016).
59. D. Mampallil, J. Reboud, R. Wilson, D. Wylie, D.R. Klug, J.M. Cooper, Soft Matter **11**, 7207 (2015).
60. F. Clément, J. Leng, Langmuir **20**, 6538 (2004).
61. F. Boulogne, F. Giorgiutti-Dauphine, L. Pauchard, Soft Matter **9**, 750 (2013).
62. C. Loussert, A. Bouchaudy, J.-B. Salmon, Phys. Rev. Fluids **1**, 084201 (2016).
63. L. Pauchard, F. Parisse, C. Allain, Phys. Rev. E **59**, 3737 (1999).
64. E. Lintingre, F. Lequeux, L. Talini, N. Tsapis, Soft Matter **12**, 7435 (2016).
65. L. Pauchard, C. Allain, Phys. Rev. E **68**, 052801 (2003).
66. Y. Gorand, L. Pauchard, G. Calligari, J.P. Hulin, C. Allain, Langmuir **20**, 5138 (2004).
67. L. Pauchard, C. Allain, C. R. Phys. **4**, 231 (2003).
68. T. Kajiyama, E. Nishitani, T. Yamaue, M. Doi, Phys. Rev. E **73**, 011601 (2006).
69. D.A. Head, Phys. Rev. E **74**, 021601 (2006).
70. L. Goehring, A. Nakahara, T. Dutta, S. Kitsunezaki, S. Tarafdar, *Desiccation cracks and their patterns: Formation and Modelling in Science and Nature* (Wiley-VCH, Singapore, 2015).
71. T. Khatun, T. Dutta, S. Tarafdar, Langmuir **29**, 15535 (2013).
72. L. Pauchard, M. Adda-Bedia, C. Allain, Y. Couder, Phys. Rev. E **67**, 027103 (2003).
73. B. Yang, J.S. Sharp, M.I. Smith, ACS Nano **9**, 4077 (2015).
74. C. Brinker, G. Scherer, *Sol-Gel Science: The Physics and Chemistry of Sol-Gel Processing* (Academic Press, New York, 1990).
75. M.A. Biot, J. App. Phys. **12**, 155 (1941).
76. L. Pauchard, B. Abou, K. Sekimoto, Langmuir **25**, 6672 (2009).
77. L. Pauchard, Europhys. Lett. **74**, 188 (2006).

78. F. Carle, D. Brutin, *Langmuir* **29**, 9962 (2013).
79. W.B. Zeid, D. Brutin, *Colloids Surf. A* **430**, 1 (2013).
80. D. Brutin, F. Carle, in *Droplet Wetting and Evaporation*, edited by D. Brutin (Academic Press, Oxford, 2015) Chapt. 19: “Droplets of colloids”, pp. 279–294.
81. L. Pauchard, F. Elias, P. Boltenhagen, A. Cebers, J.C. Bacri, *Phys. Rev. E* **77**, 021402 (2008).
82. V.R. Dugyala, H. Lama, D.K. Satapathy, M.G. Basavaraj, *Sci. Rep.* **6**, 30708 (2016).